ChemComm

COMMUNICATION

Check for updates

A superior dual functional S-scheme NiMoO₄/Mg–Al LDH heterojunction for simultaneous redox photocatalysis

Dwaipayan Dhar and Sonali Sengupta *

A heterojunction photocatalyst, NiMoO₄/Mg-Al layered-double hydroxide (LDH), was synthesized for simultaneous chloramphenicol degradation and Cr(VI) reduction under visible light. It outperformed individual components (NMO, LDH) and composites, maintaining >90% efficiency over five cycles. Synergy involved •OH/O₂⁻-mediated chloramphenicol oxidation and direct electron transfer for Cr(VI) reduction, confirmed by LC-MS and scavenger studies.

The rising occurrence of pollutants like hexavalent chromium (Cr(VI)) and chloramphenicol in water is alarming due to their high toxicity, persistence, and resistance to conventional treatments.[1] Photocatalysis has emerged as a promising strategy for the simultaneous removal of these pollutants, leveraging the ability of semiconductor materials to harness solar energy for redox reactions. Among photocatalysts, different layered double hydroxides (LDHs), particularly MgAl-LDH, have gained attention for their structural stability, high surface area, and ability to support active materials that enhance charge carrier separation and migration. The construction of heterojunctions, such as those involving NiMoO₄(NMO) and MgAl-LDH, further improves photocatalytic efficiency by facilitating charge transfer and broadening light absorption, which is crucial for the effective degradation of complex organic molecules and the reduction of toxic heavy metals under visible light. This research builds on recent advances in photocatalytic materials. It explores the synergistic effects of NiMoO₄–MgAl LDH heterojunctions for the simultaneous photocatalytic reduction of Cr(VI) and degradation of chloramphenicol. Also it aims to address the pressing need for efficient and sustainable water purification technologies.

Synthesis of the catalysts has been thoroughly described in S1.1–S1.3 of the SI. X-ray diffraction (XRD) analysis (Fig. 1a) confirmed both the phase purity and crystal structure of pure LDH, NMO and its composites at various loadings. All samples

Department of Chemical Engineering, Indian Institute of Technology Kharagpur, Kharagur, India. E-mail: sonalis@che.iitkgp.ac.in
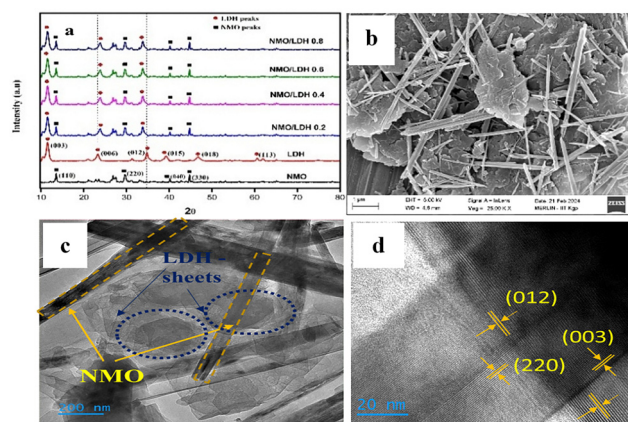

Fig. 1 (a) XRD patterns of all synthesized catalysts, (b) FESEM image of 0.6 NMO/LDH showing surface morphology, (c) HRTEM image revealing nanostructure, and (d) lattice fringe image confirming crystallinity.

showed characteristic peaks at 2θ values matching the (003), (006), (012), (015), (018), and (113) planes of (JCPDS No. 89-0460) hydrotalcite-type $Mg_6Al_2 (OH)_{18}\cdot 4.5H_2O$, indicating successful LDH synthesis.[1] Pure NMO exhibited distinct peaks at 14.2°, 29.7°, 40.5°, and 45.1°, corresponding to the (110), (220), (040), and (330) planes (JCPDS 45–0142), confirming its crystalline phase. The heterojunctions displayed peaks from both NMO and LDH, verifying effective integration and the prevalence of both in the composites. The primary exposed (012) plane and reduced LDH peak intensity for (015), (018), and (113) suggest unit cell parameter alterations. The average crystallite size of LDH was 7.84 nm with a d-spacing of 0.401 nm, calculated using the Scherrer equation.[2] Among all samples, the 0.6 NMO/LDH composite exhibited the highest crystallinity of 80.06%, compared to 77.46% for pure NMO and 73.1% for pure LDH (detailed calculation was explained in S2.1, SI).

Field-emission scanning electron microscopy (FESEM) showed that pure NMO forms uniform nanorods (80–150 nm wide), while Mg-Al LDH appears as thin, wrinkled nanosheets

(300–350 nm thick). In the NMO/LDH composites, nanorods are well-dispersed on nanosheets, especially in the 0.6 NMO/LDH sample (Fig. 1b). This results in a partially wrapped, homogeneous architecture that enhances crystallinity and potential catalytic activity. However, excessive NMO loading (0.8) causes twisted nanorods and broken sheets, indicating morphological distortion and reduced structural order. The homogeneous distribution of all the constituent elements was identified by energy dispersive X-ray spectroscopy (EDX) analysis (Fig. S1 and S2, SI).

High-resolution transmission electron microscopy (HRTEM) revealed that pristine NMO nanorods possess well-defined structures (diameters ∼100–120 nm, lengths up to several micrometres) and clear lattice fringes for the (110) plane (d-spacing ≈ 0.34 nm) (Fig. S3a, SI), confirming high crystallinity. The Mg–Al LDH nanosheets showed ultrathin, platelet-like morphology with a lattice spacing of ∼0.26 nm, matching the (003) plane (Fig. S3b, SI). In the 0.6 NMO/LDH heterojunction (Fig. 1c), intimate interfacial contact and epitaxial alignment were observed between the nanorods and nanosheets, with clear lattice fringes corresponding to both materials' characteristic planes (Fig. 1d). Selected-area electron diffraction (SAED) patterns confirmed the polycrystalline nature of both components (Fig. S3c, SI). The absence of amorphous phases and coherent lattice matching at the interface indicate successful heterostructure formation. This structural integration is expected to enhance interfacial charge transfer for catalytic applications.

All catalysts exhibited type II isotherms with H3-type hysteresis loops in Brunauer–Emmett–Teller (BET) analysis, indicating mesoporous structures with slit-like pores (Fig. S4a, SI). The 0.6 NMO/LDH heterojunction achieved the highest BET surface area (81.63 m^2 g^{-1}), outperforming pure NMO (55.12 m^2 g^{-1}), LDH (71.42 m^2 g^{-1}), and 0.8 NMO/LDH (63.06 m^2 g^{-1}). Barrett–Joyner–Halenda (BJH) analysis revealed a predominant average pore size of 25 nm, confirming well-developed mesoporosity (Fig. S4b, SI). Fourier transform infrared (FTIR) spectra of pure NMO showed characteristic peaks at 553, 722, and 969 cm^{-1}, assigned to Mo–O–Mo bending, Ni–O stretching, and Mo=O vibrations, respectively. Pure LDH exhibited peaks at 1100 and 1300 cm^{-1}, corresponding to interlayer carbonate groups. All heterojunction samples retained these distinct peaks, confirming the successful integration and structural preservation of both components (Fig. S5, SI).

X-ray photoelectron spectroscopy (XPS) analysis confirmed the presence of Ni, Mo, Mg, Al, O, and C in NMO, LDH, and NMO-LDH heterojunctions (Fig. 2a). The O 1s spectra (529.1, 532, and 533.6 eV) revealed Ni–O bonds, oxygen vacancies (Ni^{2+}), and surface hydroxyl groups, with 0.6 NMO/LDH showing enhanced O–H content, indicating superior oxygen adsorption for photochemical activity (Fig. S6a and b, SI). Ni 2p spectra exhibited peaks at 855.08–855.46 eV (Ni $2p_{3/2}$) and 870.29–870.36 eV (Ni $2p_{1/2}$), alongside the Ni(III) signatures (856.19–873.82 eV) and Ni^{2+} satellite peaks (875.3, 881.2 eV) (Fig. S6c and e, SI). Mo 3d spectra showed Mo $3d_{3/2}$ (230.37–230.83 eV) and Mo $3d_{3/2}$ (236.46–236.62 eV) states (Fig. S6d and f, SI). Negative binding energy shifts in Mo 3d and Ni 2p of the
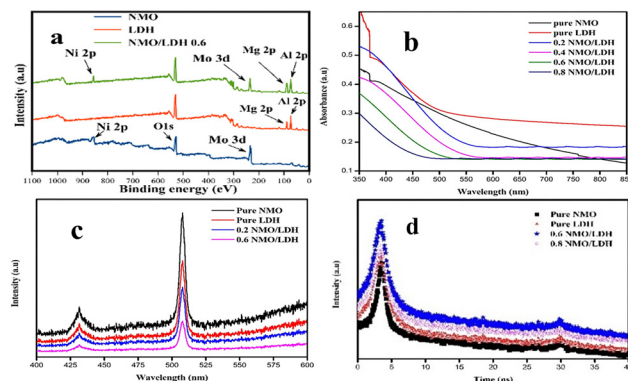

Fig. 2 (a) XPS survey spectra, (b) UV-Vis absorption spectra of the catalysts, (c) PL spectra showing charge recombination, and (d) TRPL spectra indicating carrier lifetime.

hybrid catalyst suggested strong electronic interactions between the LDH nanosheets and NMO nanorods, increasing electron density on the NMO surfaces. The Mg 1s and Al 2p spectra further validated the LDH structure (Fig. S6g–j, SI). These interfacial XPS results and the shifts in binding energy are attributed to interfacial electronic interaction or bond formation. These findings demonstrate successful heterojunction formation and explain the enhanced catalytic performance of 0.6 NMO/LDH.

The pure NMO (1.9 eV) and LDH (2.7 eV) exhibit limited visible-light activity due to suboptimal bandgaps (Fig. S7, SI). Heterojunction formation via NMO nanorod integration into LDH nanosheets reduces the bandgap progressively, with the 0.6 NMO/LDH composite achieving an optimal 2.19 eV-enabling enhanced visible-light absorption (400–650 nm, Fig. 2b). Beyond this ratio, the bandgap increases to 2.36 eV (0.8 NMO/LDH), attributed to interfacial lattice distortions that hinder charge delocalization. This trend aligns with heterojunction engineering strategies in visible-light photocatalysis, where balanced interfacial coupling minimizes recombination while preserving redox potentials for simultaneous chl degradation and Cr(VI) reduction.

The dual photoluminescence (PL) peaks (Fig. 2c) at 430 nm and 505 nm arise from distinct recombination pathways: the higher-energy peak corresponds to band-edge transitions in the NMO phase, while the lower-energy emission stems from defect states (e.g., oxygen vacancies or Mo^{5+}–O^- centres) acting as recombination traps. The 0.6 NMO/LDH heterojunction exhibits suppressed 505 nm intensity, indicating reduced defect-mediated recombination due to interfacial charge transfer between NMO and LDH. This aligns with heterojunction systems where optimized phase coupling minimizes trap states while preserving redox-active sites for charge separation. The attenuated PL intensity directly correlates with enhanced photocatalytic efficiency, as observed in analogous heterojunction architectures, where suppressed recombination enables sustained electron–hole utilization for redox reactions. The prolonged decay lifetime was determined from time-resolved photoluminescence decay analysis (TRPL) (S2.2, SI). The decay time of 10.61 ns for 0.6 NMO/LDH compared to pure NMO

(0.981 ns) and LDH (1.03 ns) suggests suppressed charge recombination due to optimized interfacial charge transfer, enhancing photocatalytic efficiency (Fig. 2d). The subsequent decrease to 7.181 ns for 0.8 NMO/LDH indicates excessive heterojunction formation, possibly introducing defect-mediated recombination pathways. This enhancement arises from the strong electronic coupling and well-matched energy levels at the heterojunction interface, which facilitate prolonged carrier lifetimes and thus improve photocatalytic performance, an effect commonly reported in advanced heterostructured photocatalysts.[3]

The photocatalytic performance of the synthesized catalysts was evaluated for simultaneous Cr(VI) reduction and chloramphenicol (chl) degradation. Among the composites, 0.6 NMO/LDH exhibited optimal activity, achieving 98.71% Cr(VI) reduction and 99.1% chloramphenicol degradation within 2 h, significantly outperforming pure NMO (Cr(VI): 0.00115 min^{-1}; chl: 0.00337 min^{-1}) and LDH (Cr(VI): 0.0032 min^{-1}; chl: 0.00373 min^{-1}) (Fig. 3).

The enhanced kinetics (Cr(VI): 0.0336 min^{-1}; chl: 0.01889 min^{-1}) for 0.6 NMO/LDH are attributed to the synergistic interfacial charge transfer enabled by the heterojunction structure, which suppresses electron–hole recombination and expands light absorption.[4] The optimal NMO loading (60%) likely maximizes interfacial contact while avoiding active site blockage, a phenomenon consistent with studies on S-scheme heterojunctions.[4] This dual functionality aligns with recent advances in LDH-based heterostructures for multifunctional photocatalytic applications.[5]

The 0.6 NMO/LDH heterojunction exhibited optimal performance at 70 mg L^{-1} catalyst loading, with efficiency declines of 21% (Cr) and 32.6% (chl) at higher loadings, likely due to aggregation-induced light scattering and reduced active site accessibility (Fig. 4a). The catalyst demonstrated remarkable sensitivity, reducing Cr(VI) at a very low concentration (0.1 ppm) completely, but the efficiency dropped to 84% at 60 ppm Cr(VI) and 44% at 70 ppm chl, suggesting active site saturation at elevated concentrations (Fig. 4b). At low concentrations (Cr: 0.1 ppm; chl: 10–50 ppm), adsorption on active sites
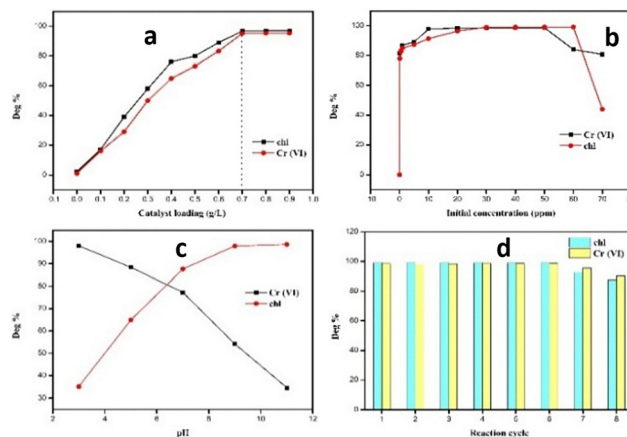

Fig. 4 Different parameters study: (a) catalyst loading, (b) initial pollutant concentration, (c) different pH, and (d) recyclability.

follows monolayer coverage, enabling efficient degradation. Beyond 60 ppm Cr(VI) and 50 ppm chl, active site saturation occurs, while light scattering by excess pollutants reduces photon penetration, both factors lowering quantum efficiency.[6] The pH-dependent behaviour of the 0.6 NMO/LDH heterojunction arises from the interplay of point of zero charge (PZC) and pollutant ionization states. The LDH component likely has a PZC >9,[7] rendering its surface positively charged below pH 9, which enhances electrostatic adsorption of Cr(VI) oxyanions (HCrO$_4^-$/Cr$_2$O$_7^{2-}$) in acidic conditions. Conversely, chl (p$K_a \sim 11$) remains predominantly neutral or weakly anionic below pH 9, limiting adsorption but favouring hydroxyl radical ($^\bullet$OH) attack at alkaline pH where $^\bullet$OH generation intensifies.[8] This creates a kinetic trade-off: Cr(VI) reduction dominates in acidic media through direct electron transfer, while alkaline conditions promote radical-driven chl degradation despite potential repulsion between the negatively charged catalyst surface and anionic drug intermediates (Fig. 4c).

The 0.6 NMO/LDH heterojunction demonstrated exceptional recyclability, retaining $>98\%$ efficiency for both Cr(VI) reduction and chl degradation over seven consecutive cycles (Fig. 4d). This performance has surpassed recent LDH-based systems (typically 3–5 cycles with $\geq 10\%$ decline).[9,10] Even after the eighth cycle, the efficiencies remained high (Cr: 90%; chl: 87%). XRD and FESEM analysis confirmed retained crystallinity and the nanorod–nanosheet morphology, indicating minimal photocorrosion or structural collapse. The gradual eighth-cycle decline aligns with partial surface hydroxyl group depletion, a reversible process addressable via brief alkaline treatment. This stability-performance synergy positions the material as a sustainable candidate for continuous wastewater treatment systems.

To elucidate the dominant reactive species in the simultaneous photocatalytic reduction of Cr(VI) and degradation of chl by 0.6 NMO/LDH, systematic radical trapping experiments were conducted using p-benzoquinone (p-BQ), EDTA-2Na, and isopropyl alcohol (IPA) as scavengers for superoxide radicals (O$_2^{\bullet-}$), holes (h$^+$), and hydroxyl radicals (OH$^\bullet$), respectively. The addition of p-BQ resulted in a pronounced decrease in Cr
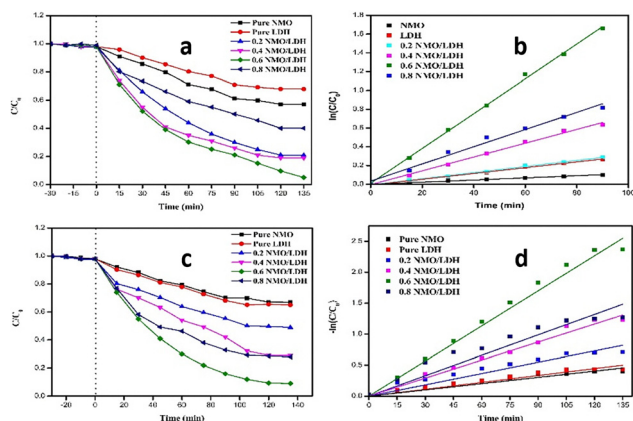

Fig. 3 (a) Cr(VI) reduction, (b) rate kinetic plot of Cr(VI) reduction, (c) chloramphenicol degradation, and (d) rate kinetic plot of chloramphenicol degradation.
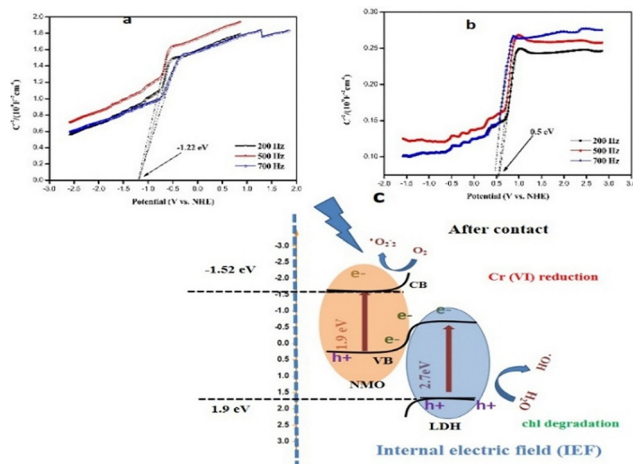
Fig. 5 Optoelectronic characterization showing (a) M–S curve of pure NMO, (b) M–S curve of pure LDH, and (c) schematic illustration of the charge-transfer mechanism.

reduction efficiency from 98% to 51.97%, indicating that $O_2^{\bullet-}$ radicals are the principal active species in the photocatalytic process (Fig. S8a, SI). In contrast, the presence of EDTA-2Na moderately reduced the chl degradation rate to 71.07%, suggesting a secondary but notable contribution from photogenerated h^+. The negligible effect of IPA confirms that $OH^{\bullet}$ plays a minimal role in this system, consistent with trends reported for other LDH-based heterojunctions where $O_2^{\bullet-}$ and h^+ dominate the reaction pathway.[11] These findings are further corroborated by EPR spectroscopy, which shows a marked increase in the $O_2^{\bullet-}$ signal under light irradiation, while no signal is observed in the dark, directly evidencing the light-driven generation of superoxide radicals as the key oxidative species. Upon irradiation, the EPR spectra for the 0.6 NMO/LDH system using DMPO as a spin-trapping agent exhibit a characteristic quartet signal for superoxide radicals ($O_2^{\bullet-}$), with a peak intensity ratio of $1:2:2:1$ (Fig. S8b, SI). This pattern directly corresponds to the hyperfine interaction of the unpaired electron with two equivalent nitrogen nuclei in the $DMPO–O_2^{\bullet-}$ adduct, confirming the formation of superoxide radicals as the primary reactive species.

Mott–Schottky (M–S) analysis confirmed the *n*-type semiconducting nature of both NMO and LDH, exhibiting flat-band potentials of -1.22 eV and -0.50 eV (*vs.* Ag/AgCl), respectively (Fig. 5a). Considering that the flat-band potential (E_{fb}) lies approximately 0.3 eV below the conduction band minimum for *n*-type semiconductors (Fig. 5b), and using Tauc plot-derived band gaps (NMO: 1.9 eV; LDH: 2.7 eV), the band edge positions were determined as CB = -1.52 eV/VB = 0.38 eV for NMO and CB = -0.80 eV/VB = 1.90 eV for LDH. This configuration forms a staggered band alignment, with the CB of NMO located below that of LDH and the VB of LDH positioned significantly higher than that of NMO—an arrangement favoring an S-scheme charge-transfer pathway rather than a conventional type-II system.[12–14] Under visible-light excitation, photogenerated electrons in the CB of LDH recombine with holes in the VB of NMO, while the remaining high-energy electrons in NMO and holes in

LDH retain strong redox potentials. Such a mechanism ensures efficient charge separation and promotes the simultaneous reduction of Cr(VI) and degradation of chloramphenicol with enhanced photocatalytic performance. The LC-MS analysis data (Fig. S9, SI) also have shown the degraded intermediates with lower *m/z* ratios, which implies the oxidation of chl.

In summary, an NMO/LDH heterojunction was developed, exhibiting exceptional visible-light-driven removal of Cr(VI) and chloramphenicol. The optimized composite achieved high efficiency through enhanced charge separation and S-scheme interfacial transfer. Mechanistic and structural studies confirmed its stability and multifunctionality. This work demonstrates a promising strategy for advanced photocatalytic water treatment.

Dwaipayan Dhar: conceptualization, writing – original draft, formal analysis, and methodology. Sonali Sengupta: writing – review and editing and supervision.

Conflicts of interest

There are no conflicts to declare.

Data availability

The data supporting this article will be made available upon request from the authors.

Data supporting the findings of this study are included in the article and in the supplementary information (SI). Supplementary information is available. See DOI: **https://doi.org/10.1039/d5cc05906b**.

References

1 J. Huang, W. Wang, T. Wu, X. Ren and X. Zhao, *RSC Adv.*, 2024, **14**, 16150–16169.
2 Y. Wang, Y. Zhang, Y. Li, Y. Zhang, H. Zhang, Z. Wang, Y. Chen and Y. Liu, *J. Mater. Chem. A*, 2024, **12**, 11230–11242.
3 Y. Wang, X. Zhang, L. Li, Z. Liu, H. Chen and J. Zhao, *Chem. Commun.*, 2025, **61**, 1164–1168.
4 Q. Zhang, Y. Wang, Y. Liu, H. Li, X. Chen and Z. Wang, *Chem. Soc. Rev.*, 2025, **54**, 4007–4052.
5 A. K. Mishra, G. C. Nayak and S. K. Pradhan, *Chem. Commun.*, 2025, **61**, 5678–5682.
6 J. Zhang, Y. Liu, L. Wang, X. Li and Z. Chen, *Chem. Soc. Rev.*, 2025, **54**, 2154–2187.
7 M. S. M. Anuar, N. H. M. Nor, S. N. Mohd Yusof, S. A. Ahmad, N. A. 5Mohd Noor, N. A. Mohd Yusof, N. H. Abdul Rahman, N. A. Mohd Nasir and N. A. Mohd Yusof, *Pharmaceutics*, 2024, **16**, 841.
8 Y. Zhang, Y. Li, S. Wang, Y. Zhang, Y. Chen and Y. Liu, *Front. Chem.*, 2018, **6**, 16.
9 Y. Zhang, J. Li, Y. Wang, S. Chen, L. Zhang, L. Wang and Y. Liu, *Nanoscale Adv.*, 2024, **6**, 3388–3398.
10 S. K. Pradhan, G. C. Nayak, A. K. Mishra, S. K. Das and S. K. Sahoo, *Environ. Sci.: Adv.*, 2024, **3**, 1121–1133.
11 Y. Zhang, J. Li, Y. Wang, S. Chen, L. Zhang, L. Wang and Y. Liu, *RSC Adv.*, 2023, **13**, 16045–16057.
12 K. Sharma, A. Sudhaik, P. Raizada, P. Thakur, X. M. Pham and Q. Van Le, *et al.*, *Environ. Sci. Pollut. Res.*, 2023, **30**, 124902–124920.
13 J. Zhang, C. Yang, H. Liu, G. Yu, Z. Duan and S. Li, *Appl. Catal., B*, 2024, **349**, 123883.
14 J. Zhang, G. Yu, C. Yang and S. Li, *Curr. Opin. Chem. Eng.*, 2024, **45**, 101040.